Extreme Mechanics Letters 51 (2022) 101604

Contents lists available at ScienceDirect

Extreme Mechanics Letters

journal homepage: www.elsevier.com/locate/eml

Magnetic soft continuum robots with contact forces

Liu Wang [a,b,c], Chuan Fei Guo [b,c], Xuanhe Zhao [a,d,*]

[a] Department of Mechanical Engineering, Massachusetts Institute of Technology, Cambridge, MA 02139, USA
[b] Centers for Mechanical Engineering Research and Education at Massachusetts Institute of Technology, Cambridge, MA 02139, USA
[c] Southern University of Science and Technology, Shenzhen 518055, China
[d] Department of Civil and Environmental Engineering, Massachusetts Institute of Technology, Cambridge, MA 02139, USA

ARTICLE INFO

Article history:
Received 3 September 2021
Accepted 3 January 2022
Available online 7 January 2022

Keywords:
Magnetic soft continuum robot
Contact force
Hard-magnetic elastica
Finite difference method
Genetic algorithm

ABSTRACT

The emerging magnetic soft continuum robots (MSCRs) – a type of slender magnetoactive soft rods that can be steered remotely by magnetic fields – hold great potential in interventional treatments of cardiovascular diseases. While forming stable contact between the distal tips of MSCRs and targeted lesions is critical in many applications such as cardiac ablations, existing designs of MSCRs have not systematically considered their contact with the external environments. In this work, we present a set of designs and optimization of MSCRs that can apply forces in contact with the environments based on theoretical modeling and numerical analysis. We propose to design MSCRs with nonuniform magnetization and nonuniform rigidity patterns so that they can achieve high steerability in the confined anatomy and apply sufficient contact forces at the targeted lesions. We first adopt the theory of hard-magnetic elastica to describe the large deflection of the MSCR with contact forces at the distal tip. We then discretize the MSCR using the finite difference method and solve for the deformation and contact forces numerically. The developed finite difference method is validated by both analytical solutions and finite element simulations. We further adopt the genetic algorithm to achieve an optimized design of the MSCR that potentially has a high steerability and capability of applying forces. Offering a facile route to analyze and optimize MSCRs with contact forces, the present work may facilitate the design of MSCRs for applications in endovascular settings.

1. Introduction

Cardiac arrhythmia such as atrial fibrillation is an irregular heart rhythm that has been an increasing epidemic and public health challenge [1,2]. To recover the normal heart rhythm, heat or cold energy is usually delivered to create tiny scars in the heart chamber to block abnormal electrical signals in the clinic, referred to as cardiac ablation [3]. Currently, most cardiac ablations are minimally invasive, in which the surgeon inserts a thin tube, also known as a mechanical catheter, into the heart chamber through the femoral artery of the patient, allowing the targeted lesion to be ablated once the catheter tip is in stable contact with the lesion. The mechanical catheter, however, is often limited by its low steerability in accessing hard-to-reach areas inside the confined anatomical environment and unprecise control of contact forces by the surgeons' hands. Excessive contact force may cause possible cardiac perforation, while insufficient contact force may lead to unsuccessful scaring [4,5]. To overcome these limitations, tremendous efforts have been dedicated to developing actively steerable catheters that can remotely perform cardiac ablations in a robotic-operated manner [6–9]. Particularly, due to the untethered and biocompatible nature of magnetic fields [10,11], an emerging minimally invasive platform that utilizes magnetic fields to control magnetoactive catheter-like rods magnetic soft continuum robots (MSCRs) has shown great promises [12–15] (Fig. 1).

An MSCR usually consists of a magneto-active distal portion that can be bent by applying an actuation magnetic field and a nonmagnetized portion that controls the MSCR's advancing and retraction (Fig. 1a). To guarantee a successful cardiac ablation, an MSCR is supposed to first steer to the targeted lesion through blood vessels and then make stable contact with the targeted lesion to create scars during the ablation [16]. The steerability of an MSCR in the confined anatomical environment is largely determined by the bending angle of its distal portion (denoted as θ_1^L in Fig. 2a), and the stability of the contact can be quantified by the contact force on the distal tip from the heart wall (denoted as $\mathbf{R}$ in Fig. 2b). Quantitative modeling of MSCRs in magnetic fields is of great importance for the understanding and control of magnetically-assisted cardiac ablation [17–24]. For example, Nelson and colleagues have applied the Cosserat rod theory to investigate the magnetically coupled behavior of a catheter with

* Corresponding author at: Department of Mechanical Engineering, Massachusetts Institute of Technology, Cambridge, MA 02139, USA.
E-mail address: zhaox@mit.edu (X. Zhao).

https://doi.org/10.1016/j.eml.2022.101604
2352-4316/

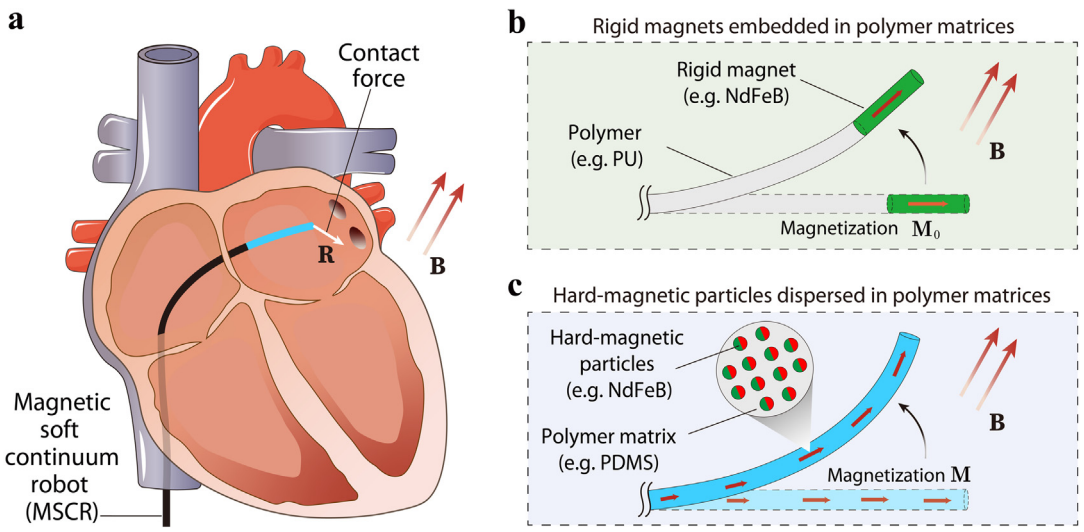

Fig. 1. (a) Schematic illustration of cardiac ablation using a magnetic soft continuum robot (MSCR) steered by the magnetic field **B**. A contact force **R** is applied by the heart wall on the tip of the MSCR to guarantee stable contact during ablation; the contact force **R** can be tuned by varying the applied magnetic field **B**. **(b)–(c)** Schematic illustration of the magneto-active distal portion of two MSCRs fabricated **(b)** by embedding rigid magnets or **(c)** by dispersing hard-magnetic particles in polymer matrices, respectively.

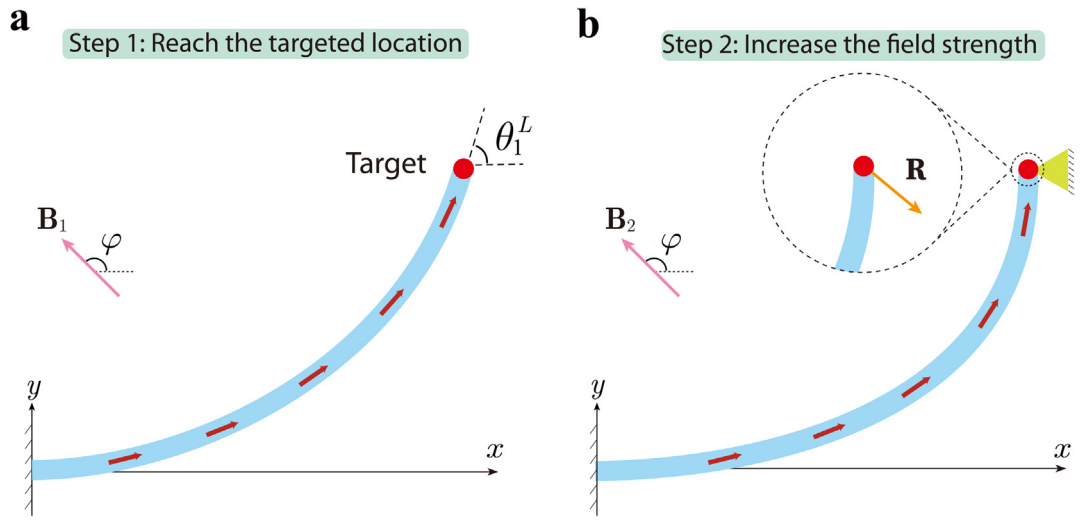

Fig. 2. A contact force **R** is applied on the distal tip of the MSCR in two steps. (a) In Step 1, the distal tip of the MSCR reaches the targeted location under a uniform magnetic field $\mathbf{B}_1$. The bending angle of the distal tip of the MSCR is denoted as θ_1^L. (b) In Step 2, the targeted location applies the contact force **R**, as the magnetic field strength increases to B_2 while maintaining the same field direction as $\mathbf{B}_1$. The objective functions to optimize the MSCR are bending angle θ_1^L and the magnitude of contact force R.

embedded rigid magnets [17] and designed a steerable magnetic sheath for cardiac ablation [18]. The contact forces between the magnet-tipped catheters and the environments have been evaluated as well [25,26]. Recently, MSCRs have been designed and optimized with a hard-magnetic elastica theory [27,28] and genetic algorithm [29] to achieve high steerability without considering contact forces. To the best of our knowledge, the design and optimization of MSCRs that can achieve both high steerability and stable contact forces at the targeted location have not been systematically investigated.

In this work, we present a set of theoretical modeling, numerical analysis, and optimization of MSCRs with contact forces under actuation magnetic fields. We propose to design MSCRs with nonuniform magnetization and rigidity patterns that can achieve both high steerability through tortuous blood vessels and the capability of applying stable contact force at the targeted location. We first adopt the theory of hard-magnetic elastica to describe the large deflection of the MSCR with contact forces at the distal end taken into account. We then discretize the MSCR using the finite difference method and solve for the deformation and contact forces numerically. The developed finite difference method is validated by both analytical solutions and finite element simulations. Enabled by the genetic algorithm, the optimized MSCR gives both a stable contact force and a higher steerability for cardiac ablation than existing MSCRs.

2. Modeling of MSCRs with contact forces

2.1. MSCRs with contact forces and their bending angles

In this study, we propose to provide precise control of contact forces between MSCRs and targeted lesions by tuning the applied magnetic field in two steps (Fig. 2). In Step 1, a uniform magnetic field $\mathbf{B}_1$ is applied to guide the MSCR to the targeted location. A larger bending angle at the distal tip (denoted as θ_1^L) indicates a higher steerability of the MSCR. After contact, we assume a

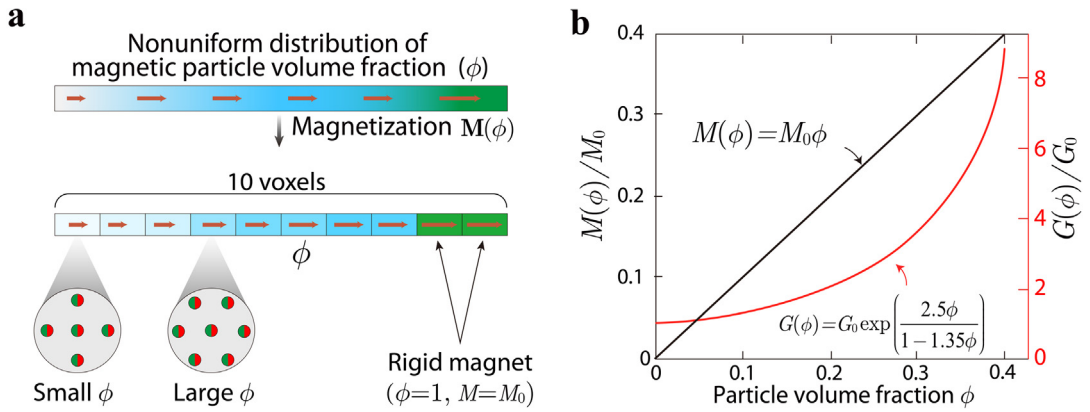

Fig. 3. Designing MSCRs by programming their magnetization and rigidity patterns in the distal portion. (a) Each voxel is encoded with a specific remanent magnetization **M** by tuning its particle volume fraction ϕ. The remanent magnetization of all voxels is along the axial direction pointing to the distal tip of the MSCR. (b) The normalized magnetization strength $M(\phi)/M_0$ (left) and shear modulus $G(\phi)/G_0$ as a function of particle volume fraction ϕ.

pin connector is formed between the distal tip and the targeted location. In Step 2, when the magnetic field strength increases to B_2, the heart wall applies a contact force (denoted as **R**) on the distal tip of the MSCR. Therefore, by tuning the magnetic field $\mathbf{B}_1$, the MSCR can reach a set of spatial locations of interest and the contact force **R** can be precisely controlled by varying the magnetic field $\mathbf{B}_2$. Note that $\mathbf{B}_1$ and $\mathbf{B}_2$ have the same direction (angle denoted as φ) so that the distal tip always contacts the targeted location during Step 2.

2.2. Design parameters for MSCRs with contact forces

The distal portions of existing MSCRs can be fabricated by embedding one or more rigid magnets [25,30–32] (Fig. 1b) or by dispersing hard-magnetic particles [29,33] (Fig. 1c) in polymer matrices (e.g., polyurethane (PU) and polydimethylsiloxane (PDMS)). Our model of the magnetoactive distal portion of the MSCR accounts for hard-magnetic particles, rigid magnets, or a combination of both (Fig. 3a). The widely adopted hard-magnetic particles and rigid magnets in MSCRs are based on neodymium–iron–boron (NdFeB) [34–36]. Once saturated by a strong magnetic field (~3 T), hard-magnetic particles can retain a remanent magnetization along the direction of the saturation magnetic field. Note that a typical actuation of MSCRs requires the magnetic field strength of at most 80 mT [33] that is much lower than the saturation field strength (~3 T) [28,37,38]. Therefore, the remanent magnetization strength of saturated hard-magnetic materials is independent of the actuation magnetic field.

It has been reported that a contact force within the range of 0.1–0.4 N is desired to improve the procedural outcome of cardiac ablation [4,5,39]. We aim to optimize the steerability of an MSCR by maximizing its bending angle θ_1^L while satisfying that the magnitude of contact force $0.1\ \text{N} \le R \le 0.4\ \text{N}$ by increasing the magnetic field strength up to 80 mT, i.e., $B_2 = 80$ mT (Fig. 2). We propose to optimize the MSCR by tuning its magnetization and rigidity patterns (Fig. 3a). The MSCR can be segmented into 10 voxels, and each voxel is encoded with a specific particle volume fraction ϕ of the hard-magnetic particle. The rigid magnet can be equivalently treated as a special case with a 100% volume fraction of hard-magnetic particles. Therefore, the design parameters are ϕ of 10 voxels, denoted as $\phi_i (i = 1, 2 \ldots 10)$. Applying a strong saturation magnetic field along the axial direction of the MSCR will produce a remanent magnetization **M** in each voxel. By tuning ϕ, the magnetization strength M and the shear modulus G of each voxel can be effectively altered (Fig. 3b). On the one hand, the magnetization strength is linearly proportional to ϕ, i.e., $M = M_0\phi$, where M_0 denotes the magnetization strength of the hard-magnetic particle. On the other hand, following the Mooney model [40], the shear modulus of the voxel follows $G = G_0 \exp[2.5\phi/(1-1.35\phi)]$ where G_0 represents the shear modulus of the polymer matrix. Notably, when $\phi = 1$, it refers to a rigid magnet with $M = M_0$ and $G \gg G_0$. Furthermore, the maximum ϕ for dispersed hard-magnetic particles in polymer matrices is found to be 0.4, above which MSCRs may not be consistently fabricated [33]. Therefore, in this study, we set that $\phi_i \in \{0, 0.1, 0.2, 0.3, 0.4, 1\}$ in which 0 represents pure polymer while 1 denotes the rigid magnet. In total, there can be $6^{10} = 60466176$ possible designs. The optimization problem can be mathematically expressed as

$$\begin{aligned} &\text{Maximize:} \quad \theta_1^L(\boldsymbol{\phi}) \\ &\text{subject to} \quad \begin{cases} \phi_i \in \{0, 0.1, 0.2, 0.3, 0.4, 1\} \\ 0.1\ \text{N} \le R(\boldsymbol{\phi}) \le 0.4\ \text{N} \\ B_1 \le B_2 = 80\ \text{mT} \end{cases} \\ &\text{where} \quad \boldsymbol{\phi} = [\phi_1, \phi_2, \ldots, \phi_{10}] \end{aligned}$$

where .

2.3. Theory of hard-magnetic elastica with contact forces

MSCRs are usually in the form of a cylindrical rod with length and cross-sectional diameter of the distal portion denoted as L and D, respectively. To describe their large deflection in a magnetic field, we adopt the theory of hard-magnetic elastica [27]. We depict the deformed distal portion of an MSCR in Step 1 and Step 2 in Fig. 4a and Fig. 4b, respectively. The MSCR is magnetized along its axial direction and the magnetization vector can be expressed as $\mathbf{M} = M\mathbf{e}_x$ in the reference configuration. When subject to the uniform magnetic fields $\mathbf{B}_1$ and $\mathbf{B}_2$, the distal portion deforms under distributed magnetic torque $\boldsymbol{\tau}_1 = \mathbf{F}_1\mathbf{M} \times \mathbf{B}_1$ and $\boldsymbol{\tau}_2 = \mathbf{F}_2\mathbf{M} \times \mathbf{B}_2$, where $\mathbf{F}_1$ and $\mathbf{F}_2$ denotes the deformation gradient in Step 1 and Step 2, respectively, and $\times$ represents the cross-product operation.

The elastica model describes the large deflection of a slender rod by its centerline and assumes that cross-sections of the rod remain perpendicular to its centerline during deformation. The cross-sectional area of the rod $A = \pi D^2/4$ and the length of the rod centerline L are assumed to be constant [41,42]. Here, we take the elastica in Step 1 as an example. The centerline can be parameterized as a spatial curve $\theta_1 = \theta_1(s)$ where s and θ_1 represents the arc length and tangential angle at the spatial point P on the elastica, respectively (Fig. 4a). Then the curvature at the point P can be calculated as

$$\kappa_1(s) = \frac{d\theta_1}{ds} \tag{1}$$

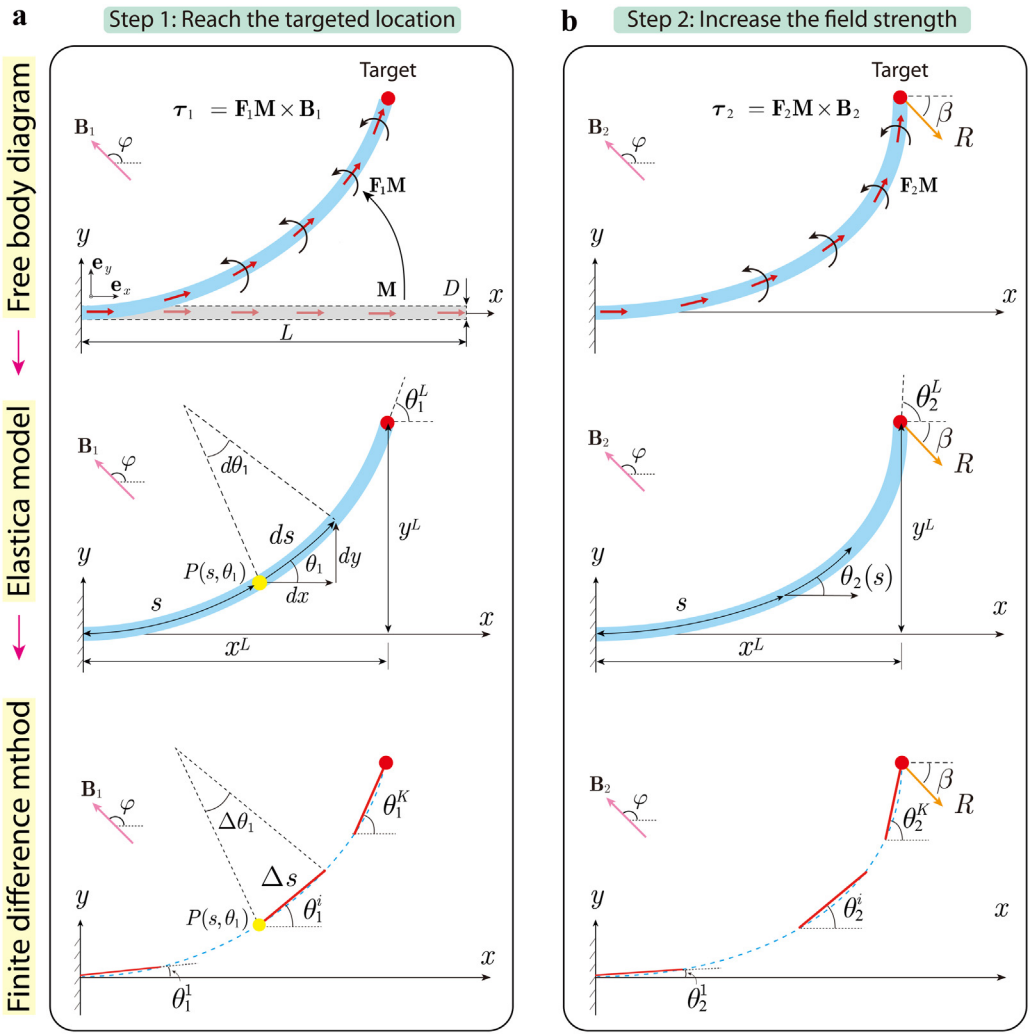

Fig. 4. Modeling the distal portion of an MSCR deforming in two steps. (a) In Step 1, the distal tip reaches the targeted location. Upper panel: Schematic illustration of the distal portion of an MSCR reaching the targeted location in the magnetic field $\mathbf{B}_1$ under distributed magnetic torque density $\boldsymbol{\tau}_1$. The length and diameter of the distal portion is denoted as L and D, respectively. Middle panel: The deformed distal portion can be characterized by a spatial curve $\theta_1(s)$, referred to as *elastica*, where s and θ_1 represents the arc length and tangential angle at the spatial point P, respectively. The bending angle and Cartesian coordinates of the distal tip is denoted as θ_1^L and (x^L, y^L), respectively. Bottom panel: The finite difference method discretizes the elastica into K elements with equal arc length $\Delta s = L/K$. (b) In Step 2, the magnetic field strength increases to B_2. Upper panel: The targeted location exerts a contact force $\mathbf{R}$ at the distal tip of the MSCR. Middle panel: The spatial curve of the deformed distal portion changes to $\theta_2(s)$ under the magnetic field $\mathbf{B}_2$. Bottom panel: Discretization of $\theta_2(s)$ with contact force $\mathbf{R}$ at the distal tip.

The deformation gradient can be expressed as

$$\begin{aligned}\mathbf{F}_1 = &\cos\theta_1\mathbf{e}_x\otimes\mathbf{e}_x + \sin\theta_1\mathbf{e}_x\otimes\mathbf{e}_y - \sin\theta_1\mathbf{e}_y\otimes\mathbf{e}_x \\ &+ \cos\theta_1\mathbf{e}_y\otimes\mathbf{e}_y + \mathbf{e}_z\otimes\mathbf{e}_z\end{aligned} \tag{2}$$

using the Cartesian coordinate basis vectors $(\mathbf{e}_x, \mathbf{e}_y, \mathbf{e}_z)$, where $\otimes$ denotes dyadic products between two vectors. The internal bending moment in the distal portion can be written as $EI\kappa_1(s)$, where $EI = 3\pi GD^4/64$ is the bending stiffness.

The targeted location is denoted as (x^L, y^L) in Fig. 4. In Step 1, the distal tip is free of external forces. Thus, the bending moment at an arbitrary point $P(x, y)$ is balanced by the summation of distributed magnetic torque $\boldsymbol{\tau}_1$ from point P to the distal tip, i.e.,

$$EIk_1(s) = EI\frac{d\theta_1}{ds} = \int_s^L \tau_1 A ds \tag{3}$$

Solving Eq. (3) with clamped boundary condition $\theta_1 = 0$ at $s = 0$ yields the deformed elastica $\theta_1(s)$. Then the Cartesian coordinates of the point P and the distal tip can be calculated

$$\begin{cases} x = \int_0^s \cos\theta_1(\eta)\,d\eta \\ y = \int_0^s \sin\theta_1(\eta)\,d\eta \end{cases} ; \quad \begin{cases} x^L = \int_0^L \cos\theta_1(\eta)\,d\eta \\ y^L = \int_0^L \sin\theta_1(\eta)\,d\eta \end{cases} \tag{4}$$

In Step 2, the contact force $\mathbf{R}$ also exerts a bending moment at point P. Therefore, the equilibrium equation can be rewritten as

$$EI\frac{d\theta_2}{ds} = \int_s^L \tau_2 A ds - R\sin\beta\left(x^L - x\right) - R\cos\beta(y^L - y) \tag{5}$$

where R is the magnitude of the contact force and β represents the angle between $\mathbf{R}$ and x-axis (Fig. 4b). Since the distal tip contacts the targeted location (i.e., (x^L, y^L) in Eq. (4)) in Step 2, we have boundary conditions at the distal tip in Step 2:

$$\begin{cases} x^L = \int_0^L \cos\theta_2(\eta)\,d\eta \\ y^L = \int_0^L \sin\theta_2(\eta)\,d\eta \end{cases} \tag{6}$$

Together with the clamped boundary condition $\theta_2 = 0$ at $s = 0$, we can solve Eq. (5) for the deformed elastica $\theta_2(s)$, the contact force R, and its direction β.

2.4. Finite difference method

For a general nonuniform magnetization pattern, Eqs. (3) and (5) can be numerically solved by the finite difference method [29]. The entire elastica is first discretized into K elements of equal length. When K is large enough, the infinitesimal arc length ds can be approximated by the straight line, i.e., $ds \approx \Delta s = L/K$ and the magnetization of each element is also a constant. In Step 1, the curvature at point P can be linearized as

$$\kappa_1(s) = \frac{d\theta_1}{ds} \approx \frac{\theta_1^i - \theta_1^{i-1}}{\Delta s} \tag{7}$$

where θ_1^i is the slope of the i_{th} element ($i = 1, 2, \ldots, K$) of the elastica $\theta_1(s)$ and $\theta_1^0 = 0$ corresponds to the clamped end at $s = 0$. Then Eq. (4) can be recast as

$$\begin{cases} x = \sum_{q=1}^{i-1} \cos\theta_1^q \Delta s \\ y = \sum_{q=1}^{i-1} \sin\theta_1^q \Delta s \end{cases} ; \quad \begin{cases} x^L = \sum_{q=1}^{K} \cos\theta_1^q \Delta s \\ y^L = \sum_{q=1}^{K} \sin\theta_1^q \Delta s \end{cases} \tag{8}$$

The distributed magnetic torque density on the i_{th} element in the magnetic field $\mathbf{B}_1$ can be calculated as $\boldsymbol{\tau}_1^i = \mathbf{F}_1\mathbf{M}_i \times \mathbf{B}_1 = M_i B_1 \sin(\varphi - \theta_1^i)\mathbf{e}_z$ where $M_i = M_0\phi_i$ is the magnetization strength of the i_{th} element. Then Eq. (3) can be written as

$$(EI)_i \frac{\theta_1^i - \theta_1^{i-1}}{\Delta s} = \sum_{q=i}^{K} AM_q B_1 \sin\left(\varphi - \theta_1^q\right) \Delta s, i = 1, 2 \ldots K \tag{9}$$

By setting $i = 1, 2 \ldots K$ in Eq. (9), we can have K equations that can be used to solve K unknowns, i.e., $\left[\theta_1^1, \theta_1^2, \ldots, \theta_1^K\right]$. Thereafter, the Cartesian coordinates of the arbitrary point $P(x, y)$ and the distal tip (x^L, y^L) can be obtained by Eq. (8).

Next, the equilibrium equation in Step 2 (i.e., Eq. (5)) can be discretized to be

$$\begin{aligned} (EI)_i \frac{\theta_2^i - \theta_2^{i-1}}{\Delta s} &= \sum_{q=i}^{K} AM_q B_2 \sin\left(\varphi - \theta_2^q\right) \Delta s - \\ R\sin\beta \sum_{q=i}^{K} \cos\theta_2^q \Delta s &- R\cos\beta \sum_{q=i}^{K} \sin\theta_2^q \Delta s, i = 1, 2 \ldots K \end{aligned} \tag{10}$$

And the coordinates of the distal tip (Eq. (6)) can be rewritten as

$$\begin{cases} x^L = \sum_{q=1}^{K} \cos\theta_2^q \Delta s \\ y^L = \sum_{q=1}^{K} \sin\theta_2^q \Delta s \end{cases} \tag{11}$$

By setting $i = 1, 2 \ldots K$ in Eq. (10), we can have K equations. Together with another 2 equations in Eq. (11), we can solve $K+2$ unknowns in Eq. (10), i.e., $\left[\theta_2^1, \theta_2^2, \ldots, \theta_2^K, R, \beta\right]$. It is worth noting that for a general nonuniform magnetization pattern, the deformed elastica $\theta_1(s)$ and $\theta_2(s)$ are different. Validation of the finite difference model is provided in Appendix.

3. Optimization by genetic algorithm

The theory of hard-magnetic elastica and finite difference method provide an effective approach for solving the bending angle (θ_1^L) of the MSCR in Step 1 and the magnitude of contact force (R) at the targeted location in Step 2. We then adopt the genetic algorithm to optimize the magnetization and rigidity pattern by tuning $\phi_i (i = 1, 2 \ldots 10)$ (Fig. 5a). Here we choose a representative polymer matrix polydimethylsiloxane (PDSM) with shear modulus $G_0 = 400$ kPa and NdFeB-based hard-magnetic particles with remanent magnetization $M_0 = 640$ kA/m [33]. The diameter and length of the distal portion are selected as $D = 3$ mm and $L = 3$ cm, respectively, which are typical values for MSCRs. First, the first generation of 100 MSCRs are randomly assigned with $\phi \in \{0, 0.1, 0.2, 0.3, 0.4, 1\}$. For each MSCR in the first generation, by setting $B_2 = 80$ mT and looping B_1 ($0 \le B_1 \le B_2$), we can calculate different bending angles θ_1^L in Step 1 and the corresponding contact forces in Step 2. Then the maximum θ_1^L that satisfies $0.1\ \text{N} \le R \le 0.4\ \text{N}$ will be recorded as the objective function of the MSCR. If the contact force does not satisfy $0.1\ \text{N} \le R \le 0.4\ \text{N}$, the objective function of the MSCR will be set to be zero. Next, by stochastic universal sampling [29], we can select 100 MSCRs from the first generation. Note that the MSCR with a larger bending angle has a higher chance to be selected (even multiple times), while the MSCR with a smaller bending angle may be eliminated during the stochastic universal sampling. Thereafter, the selected 100 MSCRs will reproduce the second generation of 100 MSCRs by 5% elitism, 85% crossover, and 10% mutation. 5% elitism means that the 5 MSCRs with the largest θ_1^L in the first generation will directly propagate to the second generation without changing the magnetization pattern (e.g., MSCR denoted as R1 in Fig. 5a). 85% crossover means that, in the remaining 95 first-generation MSCRs, we randomly choose 85 MSCRs and swap some of their voxels. For example, MSCRs denoted as R2 and R3 exchange the 1st and 100th voxels in Fig. 5a. 10% mutation means that each MSCR in the remaining 10 MSCRs will randomly alter some of its voxels. For example, MSCR denoted as R4 alters its 2nd voxel in Fig. 5a. The above optimization process of stochastic universal sampling followed by elitism, crossover, and mutation multiple times will be repeated over generations until the difference between the largest bending angle and the mean value of the all bending angles in a certain generation of MSCRs is smaller than the tolerance (10^{-3}).

Fig. 5b shows the evolution of the highest and mean values of the bending angles of 100 MSCRs over generations using the genetic algorithm. It shows that after 35 generations, the bending angles of 100 MSCRs reaches the maximum and optimal value $\theta_1^L = 161°$. The optimized magnetization pattern is plotted in Fig. 5c in which the optimal particle volume fraction of 10 voxels is $\phi = [0.2, 0, 1, 1, 1, 0, 1, 0, 1, 1]$. By setting $\varphi = 180°$, we can plot the deformed distal portion of the optimized MSCR under magnetic fields $B_1 = 10, 20, 30, 45$ mT in Fig. 5d. We also performed finite element analysis of the optimized MSCR using Abaqus 2017 standard. The interaction between the magnetic field and distributed hard-magnetic particles is simulated by implementing a user-element developed by Zhao et al. [28]. The finite element results under different magnetic fields $B_1 = 10, 20, 30, 45$ mT and $\varphi = 180°$ (shown by blue curves in Fig. 5d) agree well with the results by finite difference method, validating the finite difference method when the magnetization is nonuniform. By setting $B_2 = 80$ mT, we present the magnitude of contact force R as a function of $B_2 - B_1$ in Fig. 5e. It is found that the contact force $R \ge 0.1$ N when $B_1 \le 45$ mT. Therefore, the maximum bending angle $\theta_1^L = 161°$ is achieved when $B_1 = 45$ mT as shown in Fig. 5d.

Next, we compare the bending angles of the optimized MSCR and existing MSCRs in the literature in Fig. 6. We first analyze the

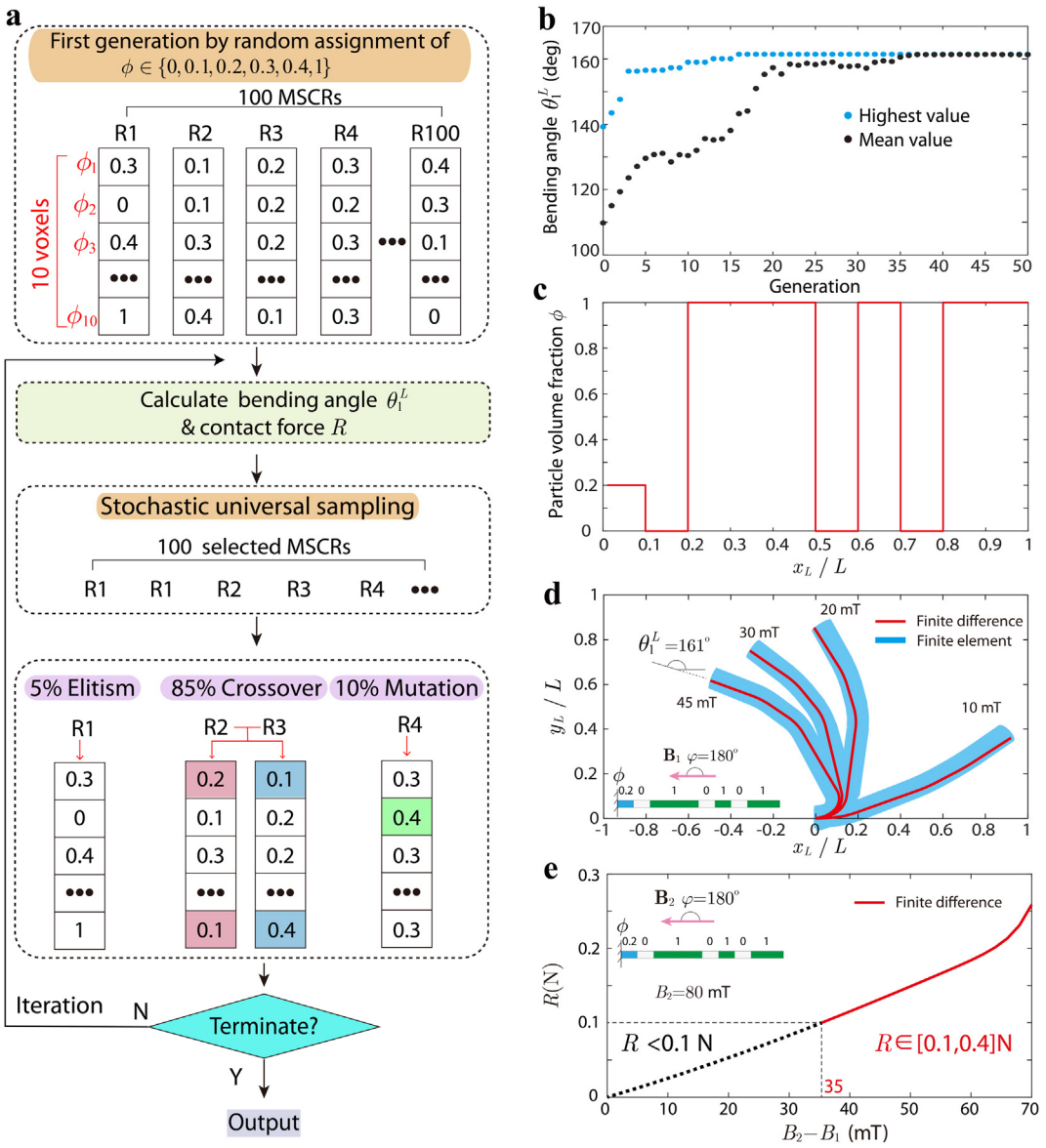

Fig. 5. Optimization of the MSCR with contact forces by genetic algorithm. (**a**) Schematic flowchart of the optimization process of MSCRs by genetic algorithm. MSCRs with a large bending angle and contact force $0.1\,\text{N} \le R \le 0.4\,\text{N}$ are selected by the stochastic universal sampling to reproduce the next generation via elitism, crossover, and mutation. (**b**) The highest and mean values of the bending angle of 100 MSCRs over generations. The bending angle reaches the maximum and optimal value of $\theta_1^L = 161°$ after 35 generations. (**c**) The hard-magnetic particle distribution of the optimized MSCR at generation 35. (**d**) Deformed profiles of the optimized MSCR in Step 1 under magnetic field $B_1 = 10, 20, 30, 45$ mT and $\varphi = 180°$ (**e**) The magnitude of contact force R as a function of $B_2 - B_1$. The maximum bending angle $\theta_1^L = 161°$ is achieved when $B_1 = 45$ mT and $\varphi = 180°$.

bending angle of MSCRs by uniformly dispersing hard-magnetic particles in polymer matrices. We found that contact forces of MSCRs with $\phi = 0.2$ [33] and $\phi = 0.4$ are smaller than 0.1 N. Next, we calculate the bending angles of four MSCRs with nonuniform distribution of hard-magnetic particles. MSCRs with linearly and parabolically decreasing particle concentration from 0.4 to 0 also have contact forces smaller than 0.1 N, while the MSCR with linearly and parabolically increasing particle concentration from 0 to 0.4 shows the maximum bending angle of 93° and 77°, respectively. The bending angles of MSCRs with contact force $R < 0.1$ N are meaningless due to unstable contact, and thus are not shown in Fig. 6.

Thereafter, we analyze the bending angles of MSCRs with embedded magnets. We first consider a single magnet embedded at the distal tip [25,32] with magnetic polarity pattern $\phi = [0, 0, 0, 0, 0, 0, 0, 0, 0, 1]$. The bending angle is calculated as 96°. Next, we analyze the MSCR with two magnets embedded in the distal portion [30,43] with magnetic polarity patterns $\phi = [0, 0, 0, 0, 1, 1, 0, 0, 1, 1]$. The bending angles is found as 145°. In contrast, enabled by the genetic algorithm, the optimized MSCR shows a bending angle of 161°, which is much larger than existing MSCRs. Notably, if we replace the voxels with $\phi = 0.2$ in the optimized design to pure polymer ($\phi = 0$), the resultant MSCR gives a maximum bending angle of 160°, suggesting that embedding rigid magnets in polymer matrices can give MSCRs with high bending angles and stable contact.

4. Conclusions

In summary, we report a strategy for the design and optimization of MSCRs that can have both a large bending angle and sufficient contact force at the targeted location. Different from existing MSCRs with either dispersed magnetic particles

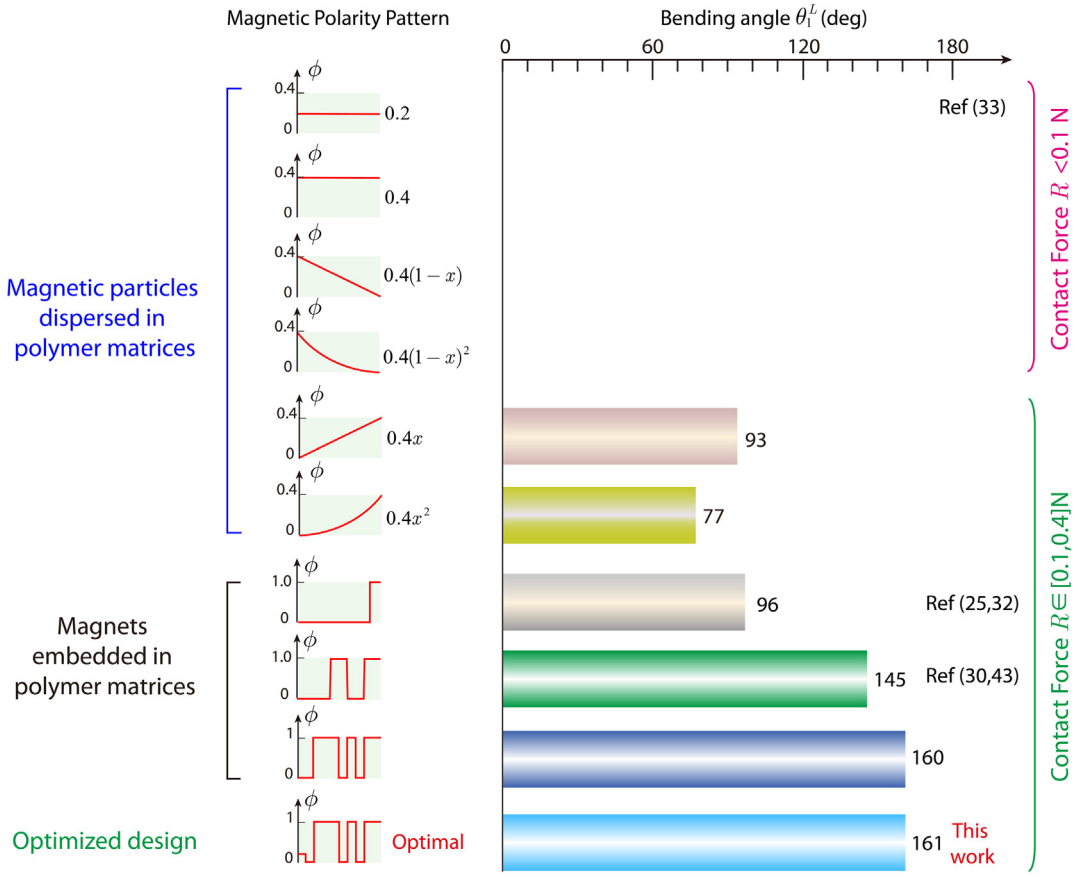

Fig. 6. Comparison of bending angles of the optimized MSCR and existing MSCRs in literature. The magnetic field strength $B_2 = 80$ mT and $\varphi = 180°$ are adopted.

or embedded rigid magnets in the polymer matrices, we propose to design MSCRs that can have both dispersed magnetic particles and embedded rigid magnets. We have developed a set of theoretical and numerical models to calculate the contact forces between MSCRs and targeted lesions actuated by uniform magnetic fields. With this method, we further adopt the genetic algorithm to optimize the MSCR. The optimized MSCR has an unintuitive magnetic polarity pattern by combining rigid magnets and dispersed magnetic particles. The optimized MSCR can give a high bending angle (e.g., up to 161°) with sufficient contact forces (e.g., 0.1∼0.4 N), implying potentially high steerability inside the confined anatomical environment and the capability of achieving stable contact with the targeted lesion in cardiac ablation. It should be noted that this work provides a simplified model of contact forces between the MSCR and the static environments. The dynamic conditions (e.g., heartbeat, blood flow, etc.) inside the heart chamber for realistic applications of magnetically controllable cardiac ablation should be further considered in future works. In addition, the current model assumes a pin connector between the distal tip and the environment. However, future studies may further consider friction and sliding between them.

CRediT authorship contribution statement

Liu Wang: Conceived the idea, Designed the work, Developed the theory, Performed the analysis, Acquired the data, Wrote and revised the paper. **Chuan Fei Guo:** Wrote and revised the paper. **Xuanhe Zhao:** Conceived the idea, Designed the work, Wrote and revised the paper, Supervised the project.

Declaration of competing interest

The authors declare that they have no known competing financial interests or personal relationships that could have appeared to influence the work reported in this paper.

Acknowledgments

The work is supported by Massachusetts Institute of Technology and by the Centers for Mechanical Engineering Research and Education at Massachusetts Institute of Technology and Southern University of Science and Technology.

Appendix A. Validation of finite difference method

When ϕ is constant throughout the distal portion, i.e., the magnetization pattern is uniform $\mathbf{M} \equiv M\mathbf{e}_x \equiv M_0\phi\mathbf{e}_x$, analytical solutions to Eqs. (3) and (5) can be derived. Therefore, we can validate the finite difference method by analytical solutions.

A.1. Analytical solutions to Eq. (3)

In Step 1, Eq. (3) can be explicitly expressed as

$$EI\frac{d\theta_1}{ds} = \int_s^L AMB_1 \sin(\varphi - \theta_1(\eta))d\eta \tag{A.1}$$

Differentiating Eq. (A.1) with respect to s yields the 2nd-order governing equation

$$EI\frac{d^2\theta_1}{ds^2} + AMB_1 \sin(\varphi - \theta_1) = 0 \tag{A.2}$$

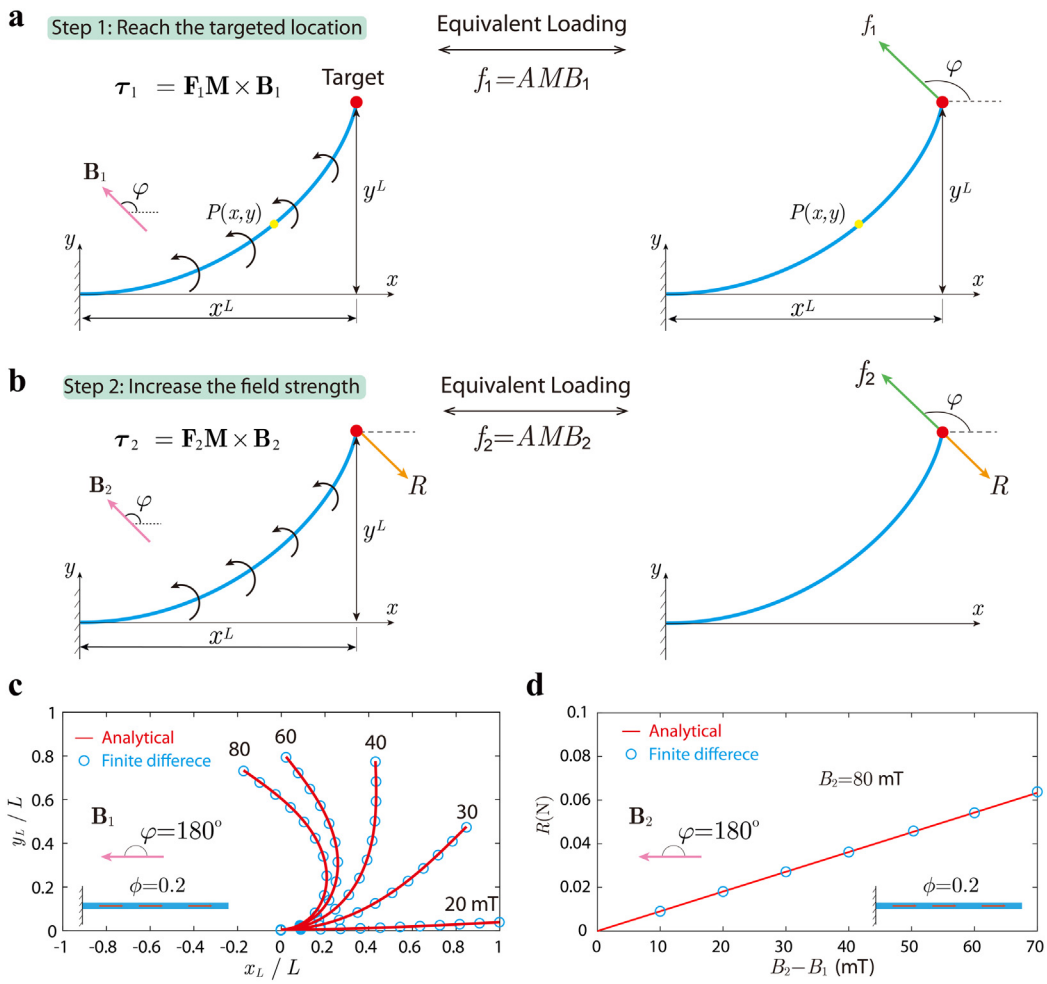

Fig. A.1. Analytical solutions when the particle volume fraction ϕ is constant. **(a)–(b)** Generalization of the distributed magnetic torque into an equivalent point force acting on the distal tip of a hard-magnetic elastica. Equivalent loading condition **(a)** $f_1 = AMB_1$ and **(b)** $f_2 = AMB_2$ yields the same deformed elastica in Step 1 and 2, respectively. **(c)–(d)** Comparison of **(c)** the deformed elastica in Step 1 and **(d)** contact forces in Step 2 between analytical solutions and results by finite difference method.

With the help of chain rule, Eq. (A.2) can be expressed in the following integral form:

$$\int \frac{d^2\theta_1}{ds^2}\frac{d\theta_1}{ds}ds = -\int Q_1 \sin(\varphi - \theta_1)ds \tag{A.3}$$

where $Q_1 = AMB_1/EI$. Integrating Eq. (A.3) produces

$$\frac{1}{2}\left(\frac{d\theta_1}{ds}\right)^2 = -Q_1\cos(\varphi - \theta_1) + C \tag{A.4}$$

The constant C can be determined from the boundary condition that there is no bending moment at the distal tip, i.e., $\theta_1'(L) = 0$, which leads to

$$C = Q_1\cos\left(\varphi - \theta_1^L\right) \tag{A.5}$$

Then Eq. (A.3) can be rearranged

$$ds = \sqrt{\frac{1}{2Q_1}}\frac{d\theta_1}{\sqrt{\cos\left(\varphi - \theta_1^L\right) - \cos(\varphi - \theta_1)}} \tag{A.6}$$

Integrating Eq. (A.6) we have

$$L = \sqrt{\frac{1}{2Q_1}}\int_0^{\theta_1^L}\frac{d\theta_1}{\sqrt{\cos\left(\varphi - \theta_1^L\right) - \cos(\varphi - \theta_1)}} = \sqrt{\frac{1}{2Q_1}}\Phi(\varphi, \theta_1^L) \tag{A.7}$$

where nondimensional function $\Phi(\varphi, \theta_1^L)$ is defined as

$$\Phi\left(\varphi, \theta_1^L\right) = \int_0^{\theta_1^L}\frac{d\theta_1}{\sqrt{\cos\left(\varphi-\theta_1^L\right)-\cos(\varphi-\theta_1)}} = \frac{2}{\sqrt{\cos\left(\varphi-\theta_1^L\right)-1}}\left[F\left(\frac{\varphi-\theta_1^L}{2}, \csc\frac{\varphi-\theta_1^L}{2}\right) - F\left(\frac{\varphi}{2}, \csc\frac{\varphi-\theta_1^L}{2}\right)\right] \tag{A.8}$$

in which F denoting the incomplete elliptic integral of the first kind defined as

$$F(\alpha, k) = \int_0^{\alpha}\frac{d\eta}{\sqrt{1 - k^2\sin 2\eta}} \tag{A.9}$$

Then Eq. (A.7) can be expressed as

$$\frac{AMB_1L^2}{EI} = \frac{1}{2}\Phi^2(\varphi, \theta_1^L) \tag{A.10}$$

Therefore, θ_1^L can be solved from Eq. (A.10). The kinematic relation of the infinitesimal arc length ds reads as

$$\begin{aligned} dx &= ds\cos\theta_1 = \sqrt{\frac{1}{2Q_1}}\frac{\cos\theta_1 d\theta_1}{\sqrt{\cos\left(\varphi-\theta_1^L\right)-\cos(\varphi-\theta_1)}} \\ dy &= ds\sin\theta_1 = \sqrt{\frac{1}{2Q_1}}\frac{\sin\theta_1 d\theta}{\sqrt{\cos\left(\varphi-\theta_1^L\right)-\cos(\varphi-\theta_1)}} \end{aligned} \tag{A.11}$$

By plugging θ_1^L into Eq. (A.11), we can solve the Cartesian coordinates of the distal tip by integrating from 0 to L, i.e.,

$$x^L = \int_0^L dx = \int_0^{\theta_1^L} \sqrt{\frac{1}{2Q_1}} \frac{\cos\theta_1 d\theta_1}{\sqrt{\cos\left(\varphi-\theta_1^L\right)-\cos(\varphi-\theta_1)}}$$
$$y^L = \int_0^L dy = \int_0^{\theta_1^L} \sqrt{\frac{1}{2Q_1}} \frac{\sin\theta_1 d\theta_1}{\sqrt{\cos\left(\varphi-\theta_1^L\right)-\cos(\varphi-\theta_1)}} \tag{A.12}$$

Appendix B. Equivalent concentrated force at the distal tip in Step 1

Now, let us consider a case in which a force $\mathbf{f}_1 = f_1(\cos\varphi\mathbf{e}_x + \sin\varphi\mathbf{e}_y)$ is acting on the distal end of the elastica in the absence of a magnetic field (Fig. A.1a). At equilibrium, the bending moment at point P can be written as

$$EI\frac{d\theta_1}{ds} = f_1\sin\varphi\left(x^L - x\right) - f_1\cos\varphi(y^L - y) \tag{B.1}$$

Differentiating Eq. (B.1) with respect to s and invoking the kinematic relation $dx = ds\cos\theta_1$ and $dy = ds\sin\theta_1$, we have

$$EI\frac{d^2\theta_1}{ds^2} + f_1\sin(\varphi-\theta_1) = 0 \tag{B.2}$$

Comparing Eqs. (A.2) and (B.2), we notice that distributed magnetic torque in the uniform magnetic field $\mathbf{B}_1$ is equivalent to a tip force

$$f_1 = AMB_1 \tag{B.3}$$

In other others, two loading conditions produce the same elastica given the same governing equation and boundary conditions.

Appendix C. Equivalent concentrated force at the distal tip in Step 2

In Step 2, when the magnetization is uniform, Eq. (5) can be explicitly expressed as

$$EI\frac{d\theta_2}{ds} = \int_s^L AMB_2\sin(\varphi-\theta_2(\eta))d\eta - R\sin\beta\left(x^L - x\right) - R\cos\beta(y^L - y) \tag{C.1}$$

Differentiating Eq. (C.1) we have

$$EI\frac{d^2\theta_2}{ds^2} + AMB_2\sin(\varphi-\theta_2) - R\sin(\beta-\theta_2) = 0 \tag{C.2}$$

Therefore, the distributed magnetic torque $\boldsymbol{\tau}_2$ can be equivalently replaced by a concentrated force $f_2 = AMB_2$. If we further set

$$R = AM(B_2 - B_1);\ \ \beta = \pi - \varphi \tag{C.3}$$

Eq. (C.2) can recover Eq. (A.2). With the same boundary conditions, i.e., clamped end at $\theta_2(0) = 0$ and moment-free $\theta_2'(L) = 0$ at the distal tip, it can be readily concluded that the deformed elastica does not change in Step 2, i.e., $\theta_2(s) = \theta_1(s)$ if Eq. (C.3) is satisfied. Therefore, the contact force R and its direction β are analytically given in Eq. (C.3).

Analytical solutions in Eq. (C.3) can be used to validate the finite difference method. Here, we choose a representative uniform magnetization with $\phi \equiv 0.2$ and discretize the distal portion into 100 elements, i.e., $K = 100$ in the finite difference method. The deformed elastica in Step 1 when $B_1 = 20, 30, 40, 60, 80$ mT and $\varphi = 180^o$ are plotted in Fig. A.1c and corresponding contact forces in Step 2 as a function of $B_2 - B_1$ are given in Fig. A.1d, respectively. Fig. A.1c–d suggest that results by finite difference method agree excellently with analytical solutions.

References

[1] G. Lippi, F. Sanchis-Gomar, G. Cervellin, Global epidemiology of atrial fibrillation: An increasing epidemic and public health challenge, Int. J. Stroke 16 (2) (2021) 217–221.

[2] A. Verma, C.-y. Jiang, T.R. Betts, J. Chen, I. Deisenhofer, R. Mantovan, L. Macle, C.A. Morillo, W. Haverkamp, R. Weerasooriya, J.-P. Albenque, S. Nardi, E. Menardi, P. Novak, P. Sanders, Approaches to catheter ablation for persistent atrial fibrillation, N. Engl. J. Med. 372 (19) (2015) 1812–1822.

[3] Y. Reddy Vivek, J. Koruth, P. Jais, J. Petru, F. Timko, I. Skalsky, R. Hebeler, L. Labrousse, L. Barandon, S. Kralovec, M. Funosako, B. Mannuva Boochi, L. Sediva, P. Neuzil, Ablation of atrial fibrillation with pulsed electric fields, JACC: Clin. Electrophysiol. 4 (8) (2018) 987–995.

[4] G. Stabile, F. Solimene, L. Calò, M. Anselmino, A. Castro, C. Pratola, P. Golia, N. Bottoni, G. Grandinetti, A. De Simone, R. De Ponti, S. Dottori, E. Bertaglia, Catheter–tissue contact force for pulmonary veins isolation: a pilot multicentre study on effect on procedure and fluoroscopy time, EP Europace 16 (3) (2013) 335–340.

[5] M. Jolaei, A. Hooshiar, J. Dargahi, M. Packirisamy, Toward task autonomy in robotic cardiac ablation: Learning-based kinematic control of soft tendon-driven catheters, Soft Robot. 8 (3) (2020) 340–351.

[6] M.N. Faddis, W. Blume, J. Finney, A. Hall, J. Rauch, J. Sell, K.T. Bae, M. Talcott, B. Lindsay, Novel, magnetically guided catheter for endocardial mapping and radiofrequency catheter ablation, Circulation 106 (23) (2002) 2980–2985.

[7] S. Ernst, F. Ouyang, C. Linder, K. Hertting, F. Stahl, J. Chun, H. Hachiya, D. Bänsch, M. Antz, K.-H. Kuck, Initial experience with remote catheter ablation using a novel magnetic navigation system, Circulation 109 (12) (2004) 1472–1475.

[8] C. Pappone, G. Vicedomini, F. Manguso, F. Gugliotta, P. Mazzone, S. Gulletta, N. Sora, S. Sala, A. Marzi, G. Augello, Robotic magnetic navigation for atrial fibrillation ablation, J. Am. Coll. Cardiol. 47 (7) (2006) 1390–1400.

[9] J.K.-R. Chun, S. Ernst, S. Matthews, B. Schmidt, D. Bansch, S. Boczor, A. Ujeyl, M. Antz, F. Ouyang, K.-H. Kuck, Remote-controlled catheter ablation of accessory pathways: results from the magnetic laboratory, Eur. Heart J. 28 (2) (2007) 190–195.

[10] S. Wu, Q. Ze, J. Dai, N. Udipi, G.H. Paulino, R. Zhao, Stretchable origami robotic arm with omnidirectional bending and twisting, Proc. Natl. Acad. Sci. 118 (36) (2021) e2110023118.

[11] M. Sitti, Miniature soft robots—road to the clinic, Nat. Rev. Mater. 3 (6) (2018) 74.

[12] N. Kumar, J. Wirekoh, S. Saba, C.N. Riviere, Y.-L. Park, Soft miniaturized actuation and sensing units for dynamic force control of cardiac ablation catheters, Soft Robot. 8 (1) (2020) 59–70.

[13] J. Hwang, J.-y. Kim, H. Choi, A review of magnetic actuation systems and magnetically actuated guidewire- and catheter-based microrobots for vascular interventions, Intell. Serv. Robot. 13 (1) (2020) 1–14.

[14] V. Tomas da, C. James Henry, L. Peter, P. Giovanni, W. Nathan James, H. Ali Kafash, A.H. Russell, V. Pietro, Challenges of continuum robots in clinical context: a review, Progr. Biomed. Eng. 2 (2020) 032003.

[15] X. Zhao, X. Chen, H. Yuk, S. Lin, X. Liu, G. Parada, Soft materials by design: Unconventional polymer networks give extreme properties, Chem. Rev. 121 (8) (2021) 4309–4372.

[16] H. Rafii-Tari, C.J. Payne, G.-Z. Yang, Current and emerging robot-assisted endovascular catheterization technologies: a review, Ann. Biomed. Eng. 42 (4) (2014) 697–715.

[17] J. Edelmann, A.J. Petruska, B.J. Nelson, Magnetic control of continuum devices, Int. J. Robot. Res. 36 (1) (2017) 68–85.

[18] C. Chautems, S. Lyttle, Q. Boehler, B.J. Nelson, Design and evaluation of a steerable magnetic sheath for cardiac ablations, IEEE Robot. Autom. Lett. 3 (3) (2018) 2123–2128.

[19] P.R. Lloyd, T. Da Veiga, A. Attanasio, N. Marahrens, J.H. Chandler, P. Valdastri, A learnt approach for the design of magnetically actuated shape forming soft tentacle robots, IEEE Robot. Autom. Lett. 5 (3) (2020) 3937–3944.

[20] C. Chautems, B.J. Nelson, The tethered magnet: Force and 5-DOF pose control for cardiac ablation, in: Proc. 2017 IEEE International Conference on Robotics and Automation, ICRA, pp. 4837–4842.

[21] T.G. Sano, M. Pezzulla, P.M. Reis, A Kirchhoff-like theory for hard magnetic rods under geometrically nonlinear deformation in three dimensions, J. Mech. Phys. Solids (2021) 104739.

[22] D. Yan, A. Abbasi, P.M. Reis, A comprehensive framework for hard-magnetic beams: Reduced-order theory, 3D simulations, and experiments, Int. J. Solids Struct. (2021) 111319.

[23] S. Jeon, A.K. Hoshiar, K. Kim, S. Lee, E. Kim, S. Lee, J.Y. Kim, B.J. Nelson, H.J. Cha, B.J. Yi, H. Choi, A magnetically controlled soft microrobot steering a guidewire in a three-dimensional phantom vascular network, Soft Robot. 6 (1) (2019) 54–68.
[24] W. Chen, Z. Yan, L. Wang, On mechanics of functionally graded hard-magnetic soft beams, Internat. J. Engrg. Sci. 157 (2020) 103391.
[25] S.L. Charreyron, Q. Boehler, A.N. Danun, A. Mesot, M. Becker, B.J. Nelson, A magnetically navigated microcannula for subretinal injections, IEEE Trans. Biomed. Eng. 68 (1) (2021) 119–129.
[26] D. Lin, J. Wang, N. Jiao, Z. Wang, L. Liu, A flexible magnetically controlled continuum robot steering in the enlarged effective workspace with constraints for retrograde intrarenal surgery, Adv. Intell. Syst. (2021) 2000211.
[27] L. Wang, Y. Kim, C.F. Guo, X. Zhao, Hard-magnetic elastica, J. Mech. Phys. Solids 142 (2020) 104045.
[28] R. Zhao, Y. Kim, S.A. Chester, P. Sharma, X. Zhao, Mechanics of hard-magnetic soft materials, J. Mech. Phys. Solids 124 (2019) 244–263.
[29] L. Wang, D. Zheng, P. Harker, A.B. Patel, C.F. Guo, X. Zhao, Evolutionary design of magnetic soft continuum robots, Proc. Natl. Acad. Sci. 118 (21) (2021) e2021922118.
[30] S. Jeon, A.K. Hoshiar, S. Kim, S. Lee, E. Kim, S. Lee, K. Kim, J. Lee, J.-y. Kim, H. Choi, Improving guidewire-mediated steerability of a magnetically actuated flexible microrobot, Micro Nano Syst. Lett. 6 (1) (2018) 15.
[31] C. Chautems, A. Tonazzini, Q. Boehler, S.H. Jeong, D. Floreano, B.J. Nelson, Magnetic continuum device with variable stiffness for minimally invasive surgery, Adv. Intell. Syst. 2 (6) (2019) 1900086.
[32] J. Sikorski, A. Denasi, G. Bucchi, S. Scheggi, S. Misra, Vision-based 3-D control of magnetically actuated catheter using BigMag—An array of mobile electromagnetic coils, IEEE/ASME Trans. Mechatronics 24 (2) (2019) 505–516.
[33] Y. Kim, G.A. Parada, S. Liu, X. Zhao, Ferromagnetic soft continuum robots, Science Robotics 4 (33) (2019) eaax7329.
[34] N. Ebrahimi, C. Bi, D.J. Cappelleri, G. Ciuti, A.T. Conn, D. Faivre, N. Habibi, A. Hošovský, V. Iacovacci, I.S.M. Khalil, V. Magdanz, S. Misra, C. Pawashe, R. Rashidifar, P.E.D. Soto-Rodriguez, Z. Fekete, A. Jafari, Magnetic actuation methods in bio/soft robotics, 31 (11) (2021) 2005137.
[35] M. Sitti, D.S. Wiersma, Pros and cons: Magnetic versus optical microrobots, Adv. Mater. 32 (20) (2020) e1906766.
[36] H.-J. Chung, A.M. Parsons, L. Zheng, Magnetically controlled soft robotics utilizing elastomers and gels in actuation: A review, Adv. Intell. Syst. n/a (n/a) (2020) 2000186.
[37] Y. Kim, H. Yuk, R. Zhao, S.A. Chester, X. Zhao, Printing ferromagnetic domains for untethered fast-transforming soft materials, Nature 558 (7709) (2018) 274.
[38] C. Zhou, Y. Yang, J. Wang, Q. Wu, Z. Gu, Y. Zhou, X. Liu, Y. Yang, H. Tang, Q. Ling, L. Wang, J. Zang, Ferromagnetic soft catheter robots for minimally invasive bioprinting, Nature Commun. 12 (1) (2021) 5072.
[39] M. Martinek, C. Lemes, E. Sigmund, M. Derndorfer, J. Aichinger, S. Winter, H.-J. Nesser, H. Pürerfellner, Clinical impact of an open-irrigated radiofrequency catheter with direct force measurement on atrial fibrillation ablation, Pacing Clin. Electrophysiol. 35 (11) (2012) 1312–1318.
[40] M. Mooney, The viscosity of a concentrated suspension of spherical particles, J. Colloid Sci. 6 (2) (1951) 162–170.
[41] C. Armanini, F. Dal Corso, D. Misseroni, D. Bigoni, From the elastica compass to the elastica catapult: an essay on the mechanics of soft robot arm, Proc. R. Soc. Lond. Ser. A Math. Phys. Eng. Sci. 473 (2198) (2017) 20160870.
[42] J. Ciambella, A. Favata, G. Tomassetti, A nonlinear theory for fibre-reinforced magneto-elastic rods, Proc. R. Soc. Lond. Ser. A Math. Phys. Eng. Sci. 474 (2209) (2018) 20170703.
[43] A. Kafash Hoshiar, S. Jeon, K. Kim, S. Lee, J.-y. Kim, H. Choi, Steering algorithm for a flexible microrobot to enhance guidewire control in a coronary angioplasty application, Micromachines 9 (12) (2018) 617.